Three-Dimensional Ray-Based Tomographic Approach for Contactless GPR Imaging

Gianluca Gennarelli, Carlo Noviello, *Member, IEEE*, Giovanni Ludeno, Giuseppe Esposito, Francesco Soldovieri, and Ilaria Catapano, *Member, IEEE*

***Abstract*— This article proposes a 3-D imaging approach for contactless ground penetrating radar surveys. The imaging problem is formulated in the linear inverse scattering context and solved by using the singular values decomposition tool. A ray-based model accounting for the electromagnetic (EM) signal propagation into an inhomogeneous medium is developed to accurately evaluate the kernel of the integral equation to be inverted. Under the proposed model, an analysis of the spatial resolution performance is carried out as a function of the geometrical and EM parameters of the scenario. To this end, theoretical concepts based on diffraction tomography and the singular value decomposition of the scattering operator are exploited. Reconstruction results based on full-wave simulated data assess the feasibility of the imaging approach.**

***Index Terms*— Contactless ground penetrating radar (GPR), linear inverse scattering, ray-based propagation, resolution analysis.**

I. Introduction

GROUND penetrating radar (GPR) is a popular diagnostic device for subsurface exploration in different fields such as geology, geophysics, civil engineering, archeology, cultural heritage monitoring, etc. [1]. A GPR transmits an electromagnetic (EM) pulse into the ground and records the echoes reflected from the buried anomalies. Subsequently, the use of suitable data processing algorithms [1], [2], [3] provides a focused image of the subsurface scene giving information on the targets' position and shape.

Conventional GPR instrumentations are ground-coupled, i.e., they operate in contact with the probed soil and record the data along single or multiple measurement lines [1]. However, the need for investigating wide and/or hazardous areas (e.g., minefields) with an acceptable surveying time has prompted the development of contactless GPRs, i.e., systems capable of stand-off operation from the ground with a measurement quota of at least a few EM wavelengths [4]. Contactless GPRs can be mounted on different observation platforms such as vehicles [5], [6], [7], [8], [9], aircrafts [10], [11], [12], satellites [13], [14], and unmanned air vehicles (UAVs) [15], [16], [17], [18] allowing fast and efficient surveys under different illumination modalities (e.g., down-looking, side-looking, and forward-looking). Moreover, even if most contactless GPR configurations are multibistatic (i.e., they use only one transmitting (Tx)/receiving (Rx) antenna pair), multistatic measurement systems have been considered as well [7], [8], [9], [19]. An overview dealing with the state of the art on contactless GPR systems is given in [20].

Contactless GPRs pose additional challenges compared with their ground-coupled counterparts. Indeed, they collect data characterized by an increased clutter level due to the lateral surface returns and multiple reflections from the air–soil interface. Furthermore, signal distortions arise due to platform instability when the GPR is allocated over a UAV. Accordingly, as pointed out in [20], suitable filtering strategies are demanded to extract the signals backscattered by subsurface targets. Finally, from the radar-imaging viewpoint, the EM scattering model should account for wave propagation into an inhomogeneous medium made by air and the soil hosting the targets to get reliable images of the scene under investigation [2].

Usually, GPR imaging is faced by resorting to migration algorithms [21], [22]. Initially proposed for seismic imaging, migration is an efficient focusing strategy based on the Fast Fourier Transform algorithm. A similar form of ω-k migration is the diffraction tomography (DT) algorithm derived from the EM wave equation (e.g., see [23], [24]). These methods are computationally effective but work only with planar measurement domains and are unsuitable for airborne or UAV-based GPR imaging. Beamforming or matched filtering is another popular imaging approach [9]. This technique applies a complex weight to the received signals to compensate for the phase shift produced by a point target and, after, the weighted signals are summed coherently to get a reflectivity map of the scene. Another class of imaging approaches is referred to as microwave tomography (MWT) and it faces imaging as the solution of a linear EM inverse scattering problem [3], [8], [11], [20], [25], [26]. MWT approaches are inverse filtering methods that generally allow an improved spatial resolution with respect to beamforming [25]. Moreover, they can manage data collected under arbitrary measurement configurations with evenly or not spaced measurement points.

This article proposes a 3-D linear MWT approach for contactless GPR imaging. Specifically, a ray-based model accounting for the presence of the air–soil interface, i.e., a half-space reference scenario, is developed and adopted to calculate

Manuscript received 14 September 2022; revised 30 November 2022 and 13 January 2023; accepted 15 February 2023. Date of publication 1 March 2023; date of current version 9 March 2023. *(Corresponding author: Gianluca Gennarelli.)*

The authors are with the Institute for Electromagnetic Sensing of the Environment, National Research Council of Italy, 80124 Naples, Italy (e-mail: gennarelli.g@irea.cnr.it).

Digital Object Identifier 10.1109/TGRS.2023.3250740

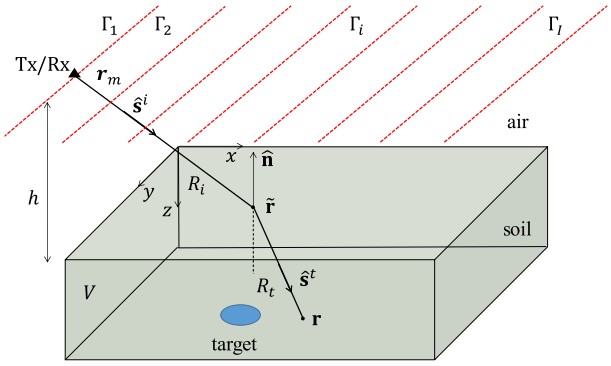

Fig. 1. Geometry of the 3-D contactless GPR imaging problem.

the kernel of the linear integral equation to be inverted. It is worth pointing out that, recently Catapano et al. [20] have proposed a scalar ray-based MWT approach for 2-D half-space scenarios. This work extends the former scalar approach to a 3-D half-space scenario by accounting for the vectorial nature of the EM scattering phenomenon. On the other hand, as shown in [27], for homogeneous reference scenarios, full-3-D imaging provides superior reconstruction capabilities compared to pseudo-3-D imaging, which is based on the combination of several 2-D reconstructions. Accordingly, the novel contribution of this article is the development of a general and flexible imaging approach that is capable of accounting for 3-D and inhomogeneous scenarios and arbitrary acquisition geometries.

Once the scattering model has been established, a thorough analysis of the achievable resolution performance is carried out by resorting to theoretical arguments of DT and with the aid of the singular value decomposition (SVD) [28] of the scattering operator. Tomographic reconstructions of extended subsurface targets achieved by inverting full-wave simulated data are reported to assess the effectiveness of the imaging approach.

The article is organized as follows. Section II provides the mathematical formulation of the imaging approach. A theoretical analysis of the reconstruction performance is presented in Section III while reconstruction results are reported in Section IV. Conclusions follow in Section V.

II. 3-D Contactless GPR Imaging Approach

A. General Formulation

We consider the geometry sketched in Fig. 1 featuring a half-space scenario where the upper region ($z < 0$) is free-space (region 1) and the lower region ($z > 0$) is a lossless, homogenous, and non-magnetic ($\mu = \mu_0 = 1.25 \times 10^{-6}$ H/m) soil (region 2) characterized by the dielectric permittivity $\varepsilon_s = \varepsilon_{rs}\varepsilon_0$, where ε_{rs} is the soil relative permittivity and $\varepsilon_0 = 8.85 \times 10^{-12}$ F/m is the free-space permittivity. The targets are supposed to be located in the subsurface investigation volume V. For sake of simplicity, the scene is probed by Tx and Rx antennas with negligible spatial offset (monostatic configuration), which record scattered field data over a measurement grid $\Gamma = \cup_{i=1}^{I}\Gamma_i$, where Γ_i are y-directed lines located at a quota h above the air–soil interface ($z = 0$). The Tx and Rx antennas are Hertzian dipoles operating in the angular frequency interval $\Omega = [\omega_{\min}, \omega_{\max}]$ and linearly polarized along the directions $\mathbf{u}_{tx}$ and $\mathbf{u}_{rx}$, respectively. We denote with $\mathbf{r}_m = (x_m, y_m, -h)$ the measurement point and $\mathbf{r} = (x, y, z)$ is a generic point in V.

At each point $\mathbf{r}$, the presence of a target is described by the contrast function [29], i.e., the variation of the target permittivity $\varepsilon(\mathbf{r})$ with respect to the soil permittivity ε_s, i.e.,

$$\chi(\mathbf{r}) = \frac{\varepsilon(\boldsymbol{r}) - \varepsilon_s}{\varepsilon_s}. \tag{1}$$

If the radar sensor is far enough (in terms of EM wavelength) from the air–soil interface, the far-field approximation holds and the wave propagation phenomena can be described by resorting to ray optics concepts [11], [20], [30]. As Fig. 1 sketches, the radar sensing process consists of the following stages.

1) A ray is emitted by the Tx antenna and travels in the air along the direction fixed by the unit vector $\hat{\mathbf{s}}^i$.
2) The ray is transmitted in the soil at the interface reflection point (IRP) $\tilde{\mathbf{r}} = (\tilde{x}, \tilde{y}, 0)$.
3) The transmitted ray travels in the subsurface along the direction fixed by the unit vector $\hat{\mathbf{s}}^t$ and a scattered field is produced when the ray encounters an EM anomaly (target).
4) Part of the scattered EM energy returns to the Rx antenna along the same path as the incident ray.

We denote with

$$R_i = \left|\tilde{\mathbf{r}} - \mathbf{r}_m\right| = \sqrt{\left(\tilde{x} - x_m\right)^2 + \left(\tilde{y} - y_m\right)^2 + h^2} \tag{2}$$

the distance between $\tilde{\mathbf{r}}$ and $\mathbf{r}_m$ along the incident ray, while

$$R_t = |\mathbf{r} - \tilde{\mathbf{r}}| = \sqrt{\left(\tilde{x} - x\right)^2 + \left(\tilde{y} - y\right)^2 + z^2} \tag{3}$$

is the distance covered by the transmitted ray from $\tilde{\mathbf{r}}$ to $\mathbf{r}$.

The EM scattering phenomenon at hand is described by resorting to the Born approximation [29]. Accordingly, the measured component of the scattered electric field along $\mathbf{u}_{rx}$ is expressed as

$$E^s(\mathbf{r}_m, \omega) = k_s^2 \iiint_V \mathbf{u}_{rx} \cdot \underline{\underline{\mathbf{G}}}^{21}(\mathbf{r}_m, \mathbf{r}) \cdot \mathbf{E}^t(\mathbf{r}, \mathbf{r}_m)\chi(\mathbf{r})d\mathbf{r}. \tag{4}$$

In (4), $k_s = \omega(\mu_0\varepsilon_s)^{1/2}$ is the propagation constant in the soil, $\mathbf{E}^t$ is the electric field transmitted in the soil at $\mathbf{r}\epsilon V$ when the $\mathbf{u}_{tx}$-polarized Tx antenna is located at $\mathbf{r}_m$, and $\underline{\underline{\mathbf{G}}}^{21}$ is the inhomogeneous dyadic Green's function accounting for the radiation from $\mathbf{r}$ to $\mathbf{r}_m$.

B. Computation of the Kernel of the Scattering Equation

In this section, the kernel of the linear integral equation (4), i.e., $\mathbf{E}^t$ and $\underline{\underline{\mathbf{G}}}^{21}$, is calculated by applying the geometrical optics (GO) theory [31]. To simplify the calculations, it is convenient to consider the local ray-fixed reference system at the IRP (see Fig. 2). Specifically, we introduce the

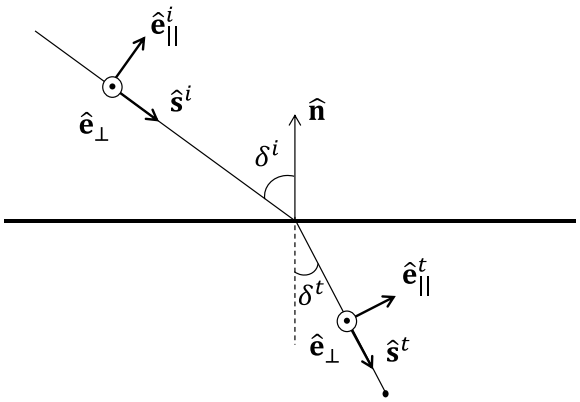

Fig. 2. Local ray-fixed reference system at the IRP.

ordinary plane of incidence Π_i as the plane defined by the incidence direction

$$\hat{\mathbf{s}}^i = \frac{(\tilde{x}-x_m)}{R_i}\hat{\mathbf{x}} + \frac{(\tilde{y}-y_m)}{R_i}\hat{\mathbf{y}} + \frac{h}{R_i}\hat{\mathbf{z}} \tag{5}$$

and the unit vector $\hat{\mathbf{n}} = -\hat{\mathbf{z}}$ normal to the air–soil interface. The local incidence angle δ^i is related to the former unit vectors by the relationship

$$\cos\delta^i = -\hat{\mathbf{s}}^i \cdot \hat{\mathbf{n}} = \hat{\mathbf{s}}^i \cdot \hat{\mathbf{z}} = \frac{h}{R_i}. \tag{6}$$

The direction of the transmitted ray is expressed by the unit vector

$$\hat{\mathbf{s}}^t = \frac{(x-\tilde{x})}{R_t}\hat{\mathbf{x}} + \frac{(y-\tilde{y})}{R_t}\hat{\mathbf{y}} + \frac{z}{R_t}\hat{\mathbf{z}}. \tag{7}$$

The electric field along the incident and transmitted rays is decomposed into the parallel (||) and perpendicular ($\perp$) components. Specifically,

$$\hat{\mathbf{e}}_\perp = \hat{\mathbf{s}}^i \times \hat{\mathbf{n}} = \frac{1}{R_i}\left[(y_m-\tilde{y})\hat{\mathbf{x}} - (x_m-\tilde{x})\hat{\mathbf{y}}\right] \tag{8}$$

is the unit vector perpendicular to the incidence plane, and

$$\begin{aligned}\hat{\mathbf{e}}^i_{||} &= \hat{\mathbf{e}}_\perp \times \hat{\mathbf{s}}^i \\ &= \frac{1}{R_i^2}\left[h(\tilde{x}-x_m)\hat{\mathbf{x}} + h(\tilde{y}-y_m)\hat{\mathbf{y}} + (h^2-R_i^2)\hat{\mathbf{z}}\right] \end{aligned} \tag{9}$$

$$\begin{aligned}\hat{\mathbf{e}}^t_{||} &= \hat{\mathbf{e}}_\perp \times \hat{\mathbf{s}}^t \\ &= \frac{1}{R_t R_i}\{z(\tilde{x}-x_m)\hat{\mathbf{x}} + z(\tilde{y}-y_m)\hat{\mathbf{y}} \\ &\quad + \left[(x_m-\tilde{x})(x-\tilde{x}) + (y_m-\tilde{y})(y-\tilde{y})\right]\}\hat{\mathbf{z}} \end{aligned} \tag{10}$$

are the unit vectors related to the parallel polarization of the incident and transmitted fields, respectively.

In the ray-fixed reference system, the amplitude of the transmitted field $\mathbf{E}^t$ at the IRP $\tilde{\mathbf{r}}$ is related to the amplitude of the incident field $\mathbf{E}^i$ at that point through the transmission coefficients matrix $\underline{\underline{\mathbf{T}}}$, i.e.,

$$\begin{bmatrix} E^t_{||} \\ E^t_\perp \end{bmatrix} = \underline{\underline{\mathbf{T}}} \cdot \begin{bmatrix} E^i_{||} \\ E^i_\perp \end{bmatrix} = \begin{bmatrix} T_{||} & 0 \\ 0 & T_\perp \end{bmatrix} \cdot \begin{bmatrix} E^i_{||} \\ E^i_\perp \end{bmatrix} \tag{11}$$

where

$$T_{||} = \frac{2\cos\delta^i}{\cos\delta^t + \sqrt{\varepsilon_{\mathrm{rs}}}\cos\delta^i} \tag{12}$$

$$T_\perp = \frac{2\cos\delta^i}{\cos\delta^i + \sqrt{\varepsilon_{\mathrm{rs}}}\cos\delta^t} \tag{13}$$

are the Fresnel's transmission coefficients for parallel and perpendicular polarization [31]. In (12) and (13), $\varepsilon_{\mathrm{rs}}$ is the relative soil permittivity and δ^t is the transmission angle, which is related to δ^i through the second Snell's law

$$\sin\delta^i = \sqrt{\varepsilon_{\mathrm{rs}}}\sin\delta^t. \tag{14}$$

According to GO [31], the transmitted field $\mathbf{E}^t$ can be expressed in the ray-fixed reference system as

$$\mathbf{E}^t(\mathbf{r}) = \begin{bmatrix} E^t_{||} \\ E^t_\perp \end{bmatrix} A(R_t)e^{-jk_sR_t} = \underline{\underline{\mathbf{T}}} \cdot \begin{bmatrix} E^i_{||} \\ E^i_\perp \end{bmatrix} A(R_t)e^{-jk_sR_t} \tag{15}$$

where

$$A(R_t) = \frac{R_i}{R_i + R_t} \tag{16}$$

is the spreading factor for the transmitted ray.

The transmitted field in (15) is rewritten in the Cartesian reference frame (see Fig. 1) by introducing the transformation matrices $\underline{\underline{\mathbf{M}}}_1$ and $\underline{\underline{\mathbf{M}}}_2$

$$\mathbf{E}^t(\mathbf{r}) = \begin{bmatrix} E^t_x \\ E^t_y \\ E^t_z \end{bmatrix} = \underline{\underline{\mathbf{M}}}_1 \cdot \underline{\underline{\mathbf{T}}} \cdot \underline{\underline{\mathbf{M}}}_2 \cdot \begin{bmatrix} E^i_x \\ E^i_y \\ E^i_z \end{bmatrix} \frac{R_i}{R_i + R_t} e^{-jk_sR_t} \tag{17}$$

in which

$$\underline{\underline{\mathbf{M}}}_1 = \begin{bmatrix} \hat{\mathbf{e}}^t_{||}\cdot\hat{\mathbf{x}} & \hat{\mathbf{e}}_\perp\cdot\hat{\mathbf{x}} \\ \hat{\mathbf{e}}^t_{||}\cdot\hat{\mathbf{y}} & \hat{\mathbf{e}}_\perp\cdot\hat{\mathbf{y}} \\ \hat{\mathbf{e}}^t_{||}\cdot\hat{\mathbf{z}} & \hat{\mathbf{e}}_\perp\cdot\hat{\mathbf{z}} \end{bmatrix} \tag{18}$$

$$\underline{\underline{\mathbf{M}}}_2 = \begin{bmatrix} \hat{\mathbf{e}}^i_{||}\cdot\hat{\mathbf{x}} & \hat{\mathbf{e}}^i_{||}\cdot\hat{\mathbf{y}} & \hat{\mathbf{e}}^i_{||}\cdot\hat{\mathbf{z}} \\ \hat{\mathbf{e}}_\perp\cdot\hat{\mathbf{x}} & \hat{\mathbf{e}}_\perp\cdot\hat{\mathbf{y}} & \hat{\mathbf{e}}_\perp\cdot\hat{\mathbf{y}} \end{bmatrix}. \tag{19}$$

The evaluation of the transmitted field in (17) involves the determination of the incident field $\mathbf{E}^i$ at the IRP for every combination of $\mathbf{r}_m$ and $\mathbf{r}$. As shown in Appendix A, the IRP is found by solving the following non-linear equation system:

$$\begin{cases} R_t^2(R_i^2-h^2) = \varepsilon_{\mathrm{rs}}R_i^2(R_t^2-z^2) \\ (\tilde{y}-y_m)x - (\tilde{x}-x_m)y - x_m\tilde{y} + y_m\tilde{x} = 0 \end{cases} \tag{20}$$

with respect to the unknown IRP coordinates $(\tilde{x},\tilde{y})$. Note that the solution of the system cannot be derived in a closed analytical form and it is found by resorting to a numerical solver for systems of non-linear equations.

The transmitted field $\mathbf{E}^t$ and the inhomogeneous dyadic Green's function $\underline{\underline{\mathbf{G}}}^{21}$ appearing in (4) write as (see Appendix B)

$$\mathbf{E}^t(\mathbf{r},\mathbf{r}_m) = -j\omega\mu_0\underline{\underline{\mathbf{M}}}_1 \cdot \underline{\underline{\mathbf{T}}} \cdot \underline{\underline{\mathbf{M}}}_2 \cdot \underline{\underline{\tilde{\mathbf{G}}}}^1 \cdot \mathbf{u}_{\mathrm{tx}} \frac{e^{-jk_0(R_i+\sqrt{\varepsilon_{\mathrm{rs}}}R_t)}}{4\pi(R_i+R_t)} \tag{21}$$

$$\underline{\underline{\mathbf{G}}}^{21}(\mathbf{r}_m,\mathbf{r}) = \underline{\underline{\tilde{\mathbf{G}}}}^{1\mathrm{T}} \cdot \underline{\underline{\mathbf{M}}}_2^T \cdot \underline{\underline{\mathbf{T}}}^T \underline{\underline{\mathbf{M}}}_1^T \frac{e^{-jk_0(R_i+\sqrt{\varepsilon_{\mathrm{rs}}}R_t)}}{4\pi(R_i+R_t)} \tag{22}$$

where the apex T denotes the transpose operation and $\underline{\underline{\tilde{\mathbf{G}}}}^1$ is defined by (B7).

C. Data Inversion

The linear integral equation in (4) is rewritten by accounting for (21) and (22) as

$$E^s(\mathbf{r}_m,\omega) = -\frac{j\omega\mu_0 k_s^2}{16\pi^2}\iiint_V \left\{\mathbf{u}_{\rm rx}\cdot\underline{\underline{\tilde{\mathbf{G}}}}^{1\rm T}\cdot\underline{\underline{\mathbf{M}}}_2^T\cdot\underline{\underline{\mathbf{T}}}^T\cdot\underline{\underline{\mathbf{M}}}_1^T \cdot\underline{\underline{\mathbf{M}}}_1\cdot\underline{\underline{\mathbf{T}}}\cdot\underline{\underline{\mathbf{M}}}_2\cdot\underline{\underline{\tilde{\mathbf{G}}}}^1\cdot\mathbf{u}_{\rm tx}\right\} \times\frac{e^{-j2k_0\left(R_i+\sqrt{\varepsilon_{rs}}R_t\right)}}{(R_i+R_t)^2}\chi(\mathbf{r})d\mathbf{r}=\mathcal{P}\chi \tag{23}$$

where $\mathcal{P}:\mathcal{L}^2(V)\rightarrow\mathcal{L}^2(\Omega\times\Gamma)$ is a linear operator projecting the unknown space onto data space.

The linear inverse problem defined by (23) is ill-posed and it is necessary to adopt a regularization strategy to get a robust solution with respect to noise on data [28]. Different schemes are available to obtain a regularized solution to the inverse problem; in this work, we exploit the truncated SVD (TSVD) [28]

$$\tilde{\chi}=\sum_{n=1}^{N_t}\frac{\langle E_S,u_n\rangle}{\sigma_n}v_n. \tag{24}$$

In the above equation, $\langle\cdot,\cdot\rangle$ stands for the scalar product in data space, $\{\sigma_n,u_n,v_n\}_{n=1}^{\infty}$ is the singular spectrum of the linear operator P, σ_n are the singular values sorted in descending order, u_n and v_n are orthonormal basis functions in the space of data and unknowns, respectively. Moreover, the truncation index N_t is the regularization parameter defining the compromise between the achievable resolution and stability of the solution [28].

The modulus of the regularized contrast function $\tilde{\chi}$ defines a spatial map here denoted as tomographic image.

III. Resolution Analysis

This section presents a comprehensive analysis of the resolution performance that can be achieved by inverting the linear model of (23). The analysis is first carried out by deriving an approximate theoretical formula for the point spread function (PSF), i.e., the reconstruction of a point-like target, based on theoretical results of DT and after in a more rigorous way with the aid of the SVD tool.

A. Approximate Theoretical Analysis

An approximate expression for the spatial resolution is obtained by exploiting DT results referred to a monostatic GPR operating in contact with the air–soil interface [2]. Specifically, when the measurement domain at the air–soil interface is a square $D=[-a,a]\times[-a,a]$ and a point target located in the middle of the investigation volume is considered, the spectral coverage of the unknown contrast function, i.e., the set of retrievable spatial harmonics, is the intersection of the regions [2]

$$\begin{cases} S_1=\left(k_x,k_y,k_z\right):k_z\geq 0\\ S_2=\left(k_x,k_y,k_z\right):k_x^2+k_y^2+k_z^2\geq 4k_{\rm min}^2\\ S_3=\left(k_x,k_y,k_z\right):k_x^2+k_y^2+k_z^2\leq 4k_{\rm max}^2\\ S_4=\left(k_x,k_y,k_z\right):k_x^2+k_y^2\leq k_z^2\tan^2\theta^* \end{cases} \tag{25}$$

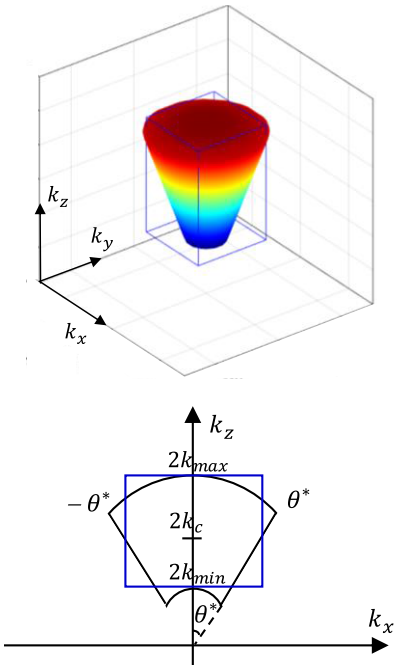

Fig. 3. Theoretical spectral set S predicted by DT in the case of a contact-based GPR and its approximating parallelepiped. (Top) 3-D view. (Bottom) View in the k_x–k_z plane.

where $k_{\rm min}$ and $k_{\rm max}$ are the minimum and maximum wavenumbers in the soil, respectively, and θ^* is the maximum illumination angle defined by the size of the measurement domain. The spectral set S in (25) is the region in the half-space $k_z\geq 0$ given by the intersection of the spherical shell with inner and outer radii $2k_{\rm min}$ and $2k_{\rm max}$ and the cone having its vertex at the origin and semi-aperture angle θ^*. A graphical representation of the spectral set S is given in Fig. 3 where the upper panel is a 3-D view while the lower panel shows a cut in the k_x–k_z plane. As seen in Fig. 3, under the limits of validity of DT, the scattering operator acts as a low pass filter along k_x and k_y and as a bandpass filter along k_z. As a result, the reconstructed contrast function $\tilde{\chi}$ is a smoothed version of the true unknown contrast χ.

As said above, the spectral set in Fig. 3 is derived for a contact GPR. However, as shown in Fig. 4 and discussed later in Section III-C, the contactless monostatic GPR configuration at hand can be managed as a contact one by considering that, for a given point target in V, the real measurement aperture at quota h maps into an "effective" aperture at the air–soil interface. Such an aperture is defined by the set of all possible IRPs by accounting for the ray paths from the measurement points to the target. Upon approximating such an effective aperture as a square in the case of a square measurement domain, the spectral coverage of the unknown contrast turns out to be defined by (25), with θ^* shown in Fig. 4.

In the following, we derive an approximate expression for the PSF. We consider an impulsive target with unit amplitude located at the point (x_0,y_0,z_0), i.e.,

$$\chi(x,y,z)=\delta(x-x_0)\delta(y-y_0)\delta(z-z_0) \tag{26}$$

where δ is the Dirac delta distribution.

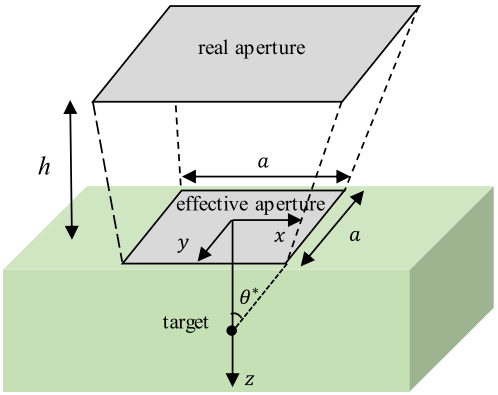

Fig. 4. Contactless GPR configuration showing the mapping of the actual measurement domain at a quota h into an effective aperture at the air–soil interface.

The PSF is defined as the inverse Fourier transform of its spectrum $\hat{\chi}(k_x, k_y, k_z)$ over the set S, i.e.,

$$\tilde{\chi}^{\mathrm{PSF}}(x, y, z) = \iiint_S \hat{\chi}(k_x, k_y, k_z) e^{-jk_x x} e^{-jk_y y} e^{-jk_z z} dk_x dk_y dk_z. \quad (27)$$

In order to get a closed formula from (29), we approximate the set S with the parallelepiped S^* (see Fig. 3)

$$S^* = (k_x, k_y, k_z) : \begin{cases} -2k_c \sin\theta^* \le k_x \le 2k_c \sin\theta^* \\ -2k_c \sin\theta^* \le k_y \le 2k_c \sin\theta^* \\ 2k_{\min} \le k_z \le 2k_{\max} \end{cases} \quad (28)$$

where k_c is the wavenumber in the soil at the central frequency.

After performing analytical calculations, the following formula is found for the PSF:

$$\tilde{\chi}^{\mathrm{PSF}}_{\mathrm{th}}(x, y, z) = \frac{64\pi B k_c^2 \sin^2\theta^*}{c} \mathrm{sinc}\left[2k_c \sin\theta^*(x - x_0)\right] \cdot \mathrm{sinc}\left[2k_c \sin\theta^*(y - y_0)\right] \times \mathrm{sinc}\left[\frac{2\pi B\sqrt{\varepsilon_{\mathrm{rs}}}}{c_0}(z - z_0)\right] \quad (29)$$

where $\mathrm{sinc}(x) = (\sin x / x)$, B is the frequency bandwidth in hertz and c_0 is the wave speed in the free-space.

From (29), it turns out that the spatial resolution limits write as

$$\Delta_x = \Delta_y = \frac{c_0}{4 f_c \sqrt{\varepsilon_{\mathrm{rs}}} \sin\theta^*} \quad (30)$$

$$\Delta_z = \frac{c_0}{2\sqrt{\varepsilon_{\mathrm{rs}}} B} \quad (31)$$

with f_c being the central frequency.

The resolution formulas in (30) and (31) are identical to those achieved in the 2-D case [30]. Moreover, in (30), the maximum illumination angle θ^* is bounded by the critical angle

$$\theta^* \le \theta^c = \sin^{-1}\left(\sqrt{\frac{1}{\varepsilon_{\mathrm{rs}}}}\right) \quad (32)$$

leading to a lower bound on the horizontal resolution

$$\Delta_{x,y} \ge \frac{c_0}{4 f_c}. \quad (33)$$

B. SVD-Based Analysis

The theoretical analysis performed in Section III-A is based on various assumptions and approximations such as the far-field condition, neglecting amplitude terms in the spectral domain (e.g., see [2]) and, last but not least, the approximation of the true spectral set S with a parallelepiped. As a result, despite the physical insight provided by (30) and (31), the resolution values they provide should be meant only as rough estimates of the true values.

A more rigorous way to estimate the resolution limits and analyze the filtering behavior of the linear operator $\mathcal{P}$ in (23) is provided by the SVD tool. More specifically, the spatial-spectral coverage of the unknown contrast function is provided by the so-called spectral content [2], [26]

$$\mathrm{SC}(k_x, k_x, k_z) = \sum_{n=1}^{N_t} \left|\hat{v}_n(k_x, k_y, k_z)\right|^2 \quad (34)$$

where $k_x, k_y,$ and k_z are the spectral variables corresponding to x, y, and z, and $\hat{v}_n(k_x, k_y, k_z)$ are the 3-D Fourier transforms of the singular functions $v_n(x, y, z)$. As shown in [32], SC represents the global (average) harmonic content of the unknown obtained by accounting for all possible positions of the point target in V.

As regards the spatial resolution, we exploit the TSVD-based expression of the PSF, i.e.,

$$\tilde{\chi}^{\mathrm{PSF}}_{\mathrm{TSVD}}(x, y, z) = \sum_{n=1}^{N_t} v_n^*(x_0, y_0, z_0) v_n(x, y, z) \quad (35)$$

where (x_0, y_0, z_0) is the position of the point target and the symbol $*$ denotes the conjugation operation.

The figures of merit in (34), and (35) do not rely on any approximation; however, they cannot be put in closed form and need to be evaluated numerically.

C. Numerical Analysis

Numerical tests aiming at assessing the achievable resolution performance are reported in the following. The tests are related to the scenario sketched in Fig. 5 featuring a lossless homogenous soil probed by a measurement grid $\Gamma = [0, 2] \times [0, 2]$ m^2 consisting of 41 y-directed lines. The measurement step along the lines and the spacing between the lines are fixed at 0.05 m. A multimonostatic/multifrequency GPR configuration is considered where the Tx and Rx antennas are Hertzian dipoles directed along x. The antennas operate in the frequency band $B = [200, 600]$ MHz, which is sampled with a uniform step equal to 50 MHz. The subsurface investigation volume $V = [0, 2] \times [0, 2] \times [0, 1]$ m^3 is discretized into voxels having parallelepiped shape and size 0.1 m along x and y and 0.05 m along z. The resolution analysis is carried out for different values of the measurement quota h and soil relative permittivity $\varepsilon_{\mathrm{rs}}$: 1) $h = 1$ m and $\varepsilon_{\mathrm{rs}} = 4$; 2) $h = 1$ m and $\varepsilon_{\mathrm{rs}} = 6$; 3) $h = 2$ m and $\varepsilon_{\mathrm{rs}} = 4$; and 4) $h = 2$ m and $\varepsilon_{\mathrm{rs}} = 6$.

Ad hoc simulation codes have been developed in the MATLAB 2019 environment. In particular, as regards the computation of the IRPs, the non-linear system in (20) has

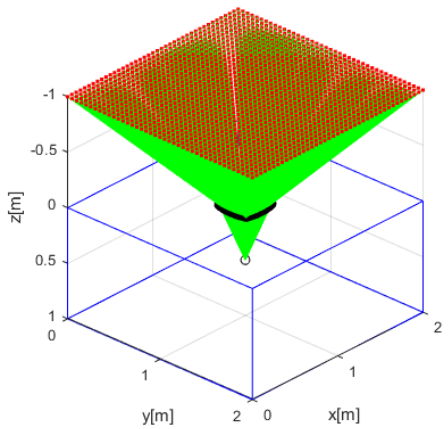

Fig. 5. Simulated scenario. The rays from the measurement points (red dots) to the target (black circle) are shown to highlight how the measurement domain maps into an effective aperture (black area) at $z = 0$.

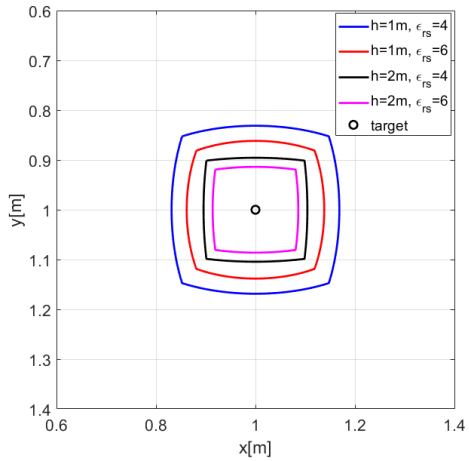

Fig. 6. Comparison between the effective apertures achieved for a point target at (1.0, 1.0, 0.5) m and different values of h and $\varepsilon_{\mathrm{rs}}$.

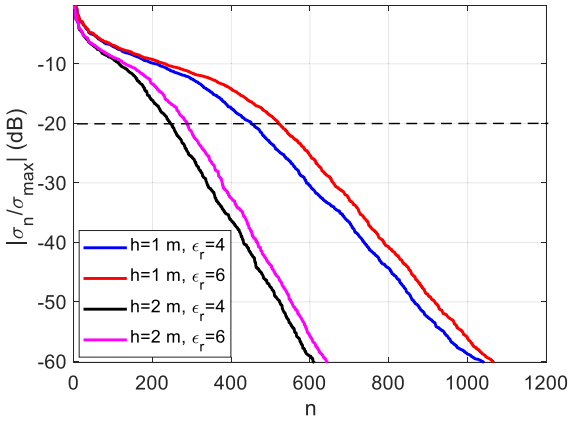

Fig. 7. Normalized singular values of the operator P expressed in decibel for different values of h and $\varepsilon_{\mathrm{rs}}$.

been solved by using the Trust-Region Dogleg Algorithm [33] implemented by the *fsolve* function. The coordinates (x, y) of the generic voxel in V are given in input to the solver as starting point to search for the solution.

A point target is considered in the middle of the investigated volume at (1.0, 1.0, 0.5) m as seen in Fig. 5. The green lines represent the paths of the rays from the measurement points to the target undergoing refraction at the IRPs. These last define a region (black area) at the air–soil interface that has been defined as an effective aperture in Section III-A. The IRPs can be treated as virtual sources illuminating the target and, consequently, the effective aperture can be regarded as a virtual measurement domain probing the target. Note that, based on (30), the horizontal resolution depends on the effective aperture size through the maximum illumination angle θ^* (see Fig. 4).

Fig. 6 provides an interesting comparison between the effective apertures achieved for the different values of h and $\varepsilon_{\mathrm{rs}}$. Due to the symmetry of the actual measurement domain with respect to the target, the effective apertures also preserve the symmetry; however, their shape and size are sensitive to the parameter values. Specifically, when the measurement domain is closer to the air–soil interface ($h = 1$ m), the contour of the effective aperture exhibits a larger curvature. Moreover, for a fixed h, increasing $\varepsilon_{\mathrm{rs}}$ turns into a reduction of the effective aperture area. A similar phenomenon is observed also when h grows at parity of $\varepsilon_{\mathrm{rs}}$.

The curves plotted in Fig. 7 display the trend of the singular values of the operator $\mathcal{P}$ for the considered values of h and $\varepsilon_{\mathrm{rs}}$. As expected, regardless of the parameters' values, the curves exhibit a rapid decay as the index n grows. However, for a fixed TSVD threshold (-20 dB in Fig. 7), the curves referred to $h = 2$ m experience a faster decay than that observed for $h = 1$ m. This outcome suggests a worse resolution performance for increasing value of h, because fewer singular values contribute to the reconstruction of the unknown contrast function [see (26)].

The curves in Fig. 7 also reveal that, for a fixed value of h, the number of retained singular values is slightly larger for soil with a higher permittivity. Therefore, in this case, soil permittivity helps improve the spatial resolution. Indeed, as it will be shown later, increasing the permittivity mostly provides a resolution enhancement along depth as also suggested by (31).

To visualize the effect of the parameters on the spatial resolution, the PSF has been evaluated based on (35) by setting the TSVD threshold at -20 dB. The cuts along x, y, and z of the PSF amplitude normalized to their maxima are illustrated in the left, middle, and right panels of Fig. 8, respectively. Different considerations can be made based on these graphs. First, the cuts along x and y of the PSF are identical as also predicted by the approximate formula of the PSF [see (29)]. These cuts highlight that, for a fixed value of h, resolutions along x and y are invariant with respect to $\varepsilon_{\mathrm{rs}}$. An explanation of this result can be given by considering that the effective aperture size (i.e., the maximum illumination angle) decreases when $\varepsilon_{\mathrm{rs}}$ grows (see Fig. 6). As a result, upon considering (30), the increase of $\varepsilon_{\mathrm{rs}}$ is balanced by the reduction of θ^* and the horizontal resolution does not vary. On the other hand, for a fixed $\varepsilon_{\mathrm{rs}}$, the horizontal resolution worsens notably when h grows. This result agrees with the curves of singular values plotted in Fig. 7 and is also predicted by (30) given the

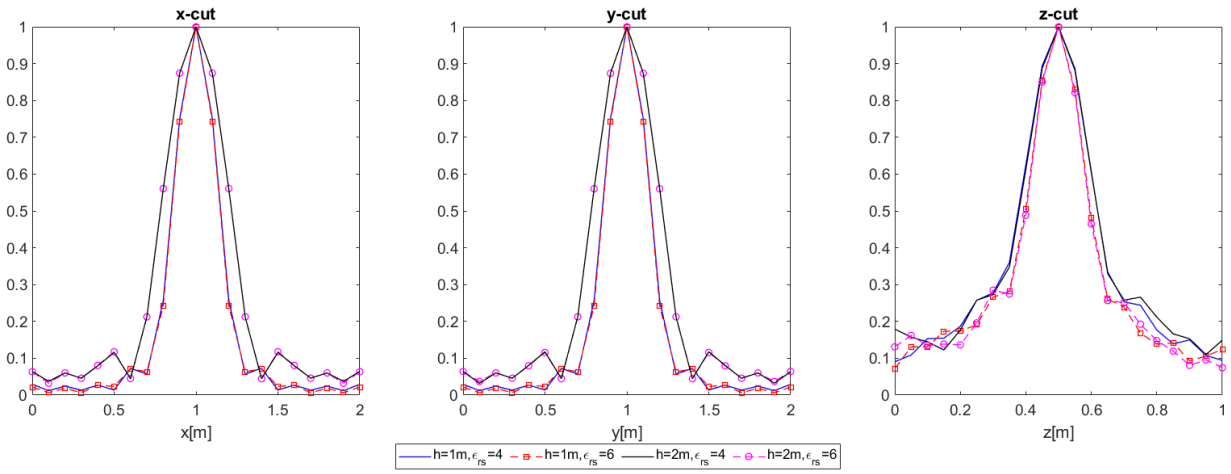

Fig. 8. Comparison of the normalized PSF amplitude cuts related to a point target at (1.0, 1.0, 0.5) m for the different values of h and $\varepsilon_{\rm rs}$. (Left) x-cut. (Middle) y-cut. (Right) z-cut.

TABLE I
RESOLUTION RESULTS FOR A POINT TARGET AT (1.0, 1.0, 0.5) m

Case	Resolution [m]	TSVD-based values [m]	Theoretical values [m]
h=1 m, ε_{rs}=4	Δx	0.22	0.26
	Δy	0.22	0.26
	Δz	0.17	0.17
h=1 m, ε_{rs}=6	Δx	0.22	0.26
	Δy	0.22	0.26
	Δz	0.14	0.13
h=2 m, ε_{rs}=4	Δx	0.32	0.40
	Δy	0.32	0.40
	Δz	0.17	0.17
h=2 m, ε_{rs}=6	Δx	0.32	0.40
	Δy	0.32	0.40
	Δz	0.14	0.13

TABLE II
RESOLUTION FOR A POINT TARGET AT $x = 1.0$ m AND $y = 1.0$ m VERSUS DEPTH

Case	Resolution [m]	TSVD-based values [m]	Theoretical values [m]
z=0.2 m	Δx	0.22	0.24
	Δy	0.22	0.24
	Δz	0.13	0.13
z=0.5 m	Δx	0.22	0.26
	Δy	0.22	0.26
	Δz	0.13	0.13
z=0.8 m	Δx	0.23	0.27
	Δy	0.23	0.27
	Δz	0.13	0.13

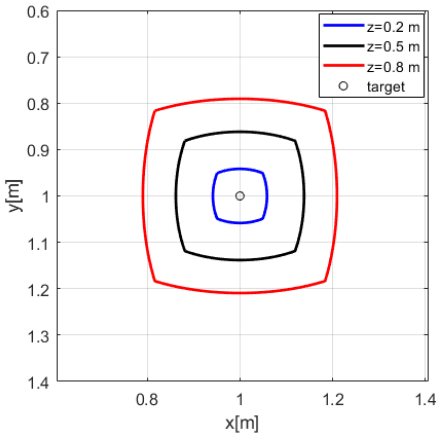

Fig. 9. Equivalent apertures for targets located at varying depths when $h = 1$ m and $\varepsilon_{\rm rs} = 6$.

reduction of the effective aperture size (i.e., θ^*) observed in Fig. 6. The right panel of Fig. 8 also highlights that depth resolution is independent on h and, for a fixed h, it increases with $\varepsilon_{\rm rs}$ in agreement with (31).

A quantitative assessment of the imaging performance is carried out by evaluating the resolution values from the PSF following the -3 dB (i.e., half power) criterion. Table I summarizes the TSVD-based resolution data confirming the previous considerations and a quite good agreement with the theoretical values provided by (30) and (31). Note that these last values are referred to the first null of the sinc$(\cdot)$ function; accordingly, they are converted to -3 dB resolution values by applying the scaling factor of 0.9.

In the following, we investigate the effect of the target depth on the resolution. The measurement quota and the soil permittivity are set as $h = 1$ m and $\varepsilon_{\rm rs} = 6$, respectively, and the target is centered in the xy plane at depths as $z = 0.2$, 0.5, and 0.8 m. The effective apertures achieved for each depth value are depicted in Fig. 9. A smaller effective aperture is attained when the target is located in the proximity of the surface; conversely deeper targets are illuminated by a larger effective aperture.

The cuts of the normalized PSF and the corresponding resolution data versus the target's depth are reported in Fig. 10 and Table II, respectively. The achieved results confirm that the horizontal resolution does not vary significantly with the target depth. Indeed, despite the effective aperture area increasing with the depth (see Fig. 9), the illumination angle θ^* appearing in (30) does not vary significantly because the depth also increases. As for the resolution along z, its value is not affected by the target depth and is determined only by the radar system bandwidth when the soil permittivity is fixed.

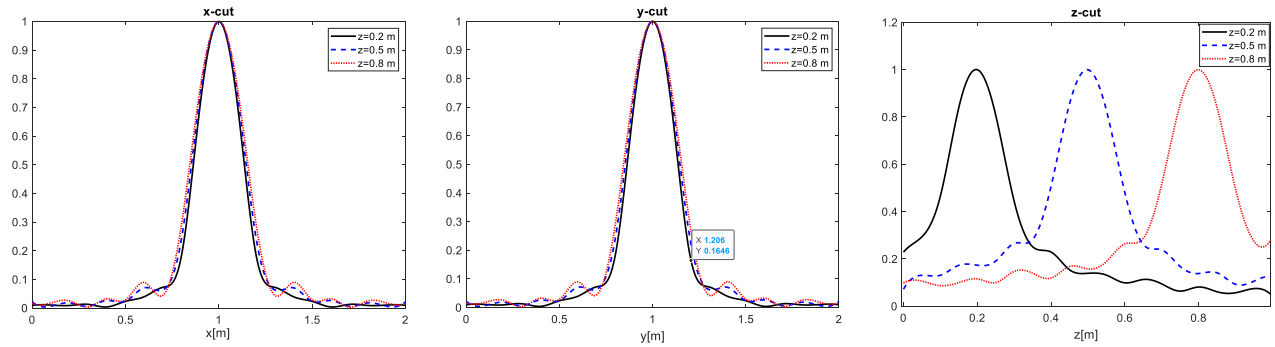

Fig. 10. Comparison of the PSF cuts related to target at depth $z = 0.2$, 0.5, and 0.8 m. (Left) x-cut. (Middle) y-cut. (Right) z-cut.

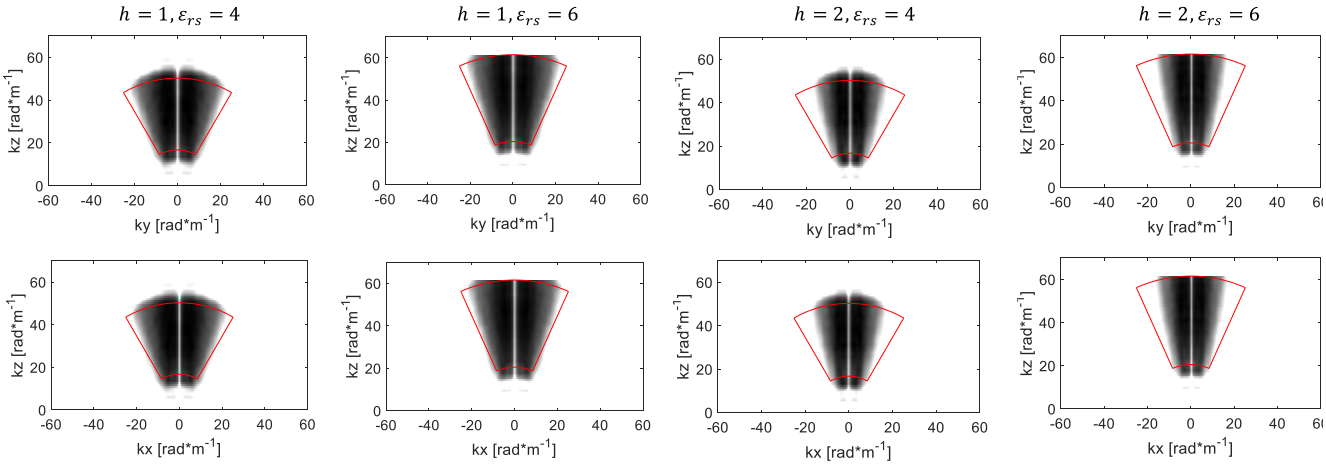

Fig. 11. Cuts of the normalized spectral content in decibel for the different values of h and $\varepsilon_{\mathrm{rs}}$. (Top) k_x-cut. (Bottom) k_y-cut. The red curve lines delimit the theoretical spectral set in (35). Dynamic range $[-10, 0]$ dB.

We conclude the resolution analysis by showing in Fig. 11 the cuts of the TSVD-based spectral content evaluated according to (34). The spectral set in (25) referred to the critical angle θ^c is also shown to highlight the maximum amount of information that can be theoretically retrieved. Note that, the TSVD-based spectral content does not match exactly the theoretical set because the condition $\theta^* = \theta^c$ is rarely verified save for measurement points on the edge of the measurement domain. Despite that, the trend of the spectral content versus h and $\varepsilon_{\mathrm{rs}}$ is coherent with resolution results retrieved from the PSF analysis. Indeed, increasing h at parity of $\varepsilon_{\mathrm{rs}}$ reduces the harmonic content along the k_x and k_y due to the reduced effective aperture size (see Fig. 6). On the other hand, when $\varepsilon_{\mathrm{rs}}$ grows at parity of h, we observe a clear increase of the harmonic content along k_z, which is related to an increase of the resolution along depth [see (31)].

IV. Reconstruction Results

Tomographic reconstructions obtained from full-wave synthetic data are reported in this section to assess the performance of the proposed imaging approach for the case of extended targets. To this aim, the EM simulator GPRMAx [34] is exploited to generate electric field data with x-directed Hertzian dipoles radiating a Ricker wavelet centered at the frequency of 400 MHz. The model parameters including soil permittivity, measurement grid, investigation domain, and TSVD threshold are identical to those used for the resolution analysis in Section III. Two diverse scenarios are considered here as shown in Fig. 12. The first scenario (left panel of Fig. 12) features an L-shaped cavity ($\varepsilon_{\mathrm{rs}} = 1$) with thickness along z equal to 0.1 m and buried at a depth of 0.45 m with respect to the air–soil interface. The second scenario (middle panel in Fig. 12) comprises the L-shaped target and a cubic cavity with the size of $0.3 \times 0.3 \times 0.2$ m buried at a depth of 0.55 m. The positions and the size of the two considered targets in the xy plane are indicated in the right panel of Fig. 12.

Electric field (x-component) radargrams are calculated over the fast-time window [0, 60] ns and processed by the following operations: zero time setting at 2.98 ns and time-gating up to 14 ns to reject the direct coupling between the Tx and Rx antennas and the reflection from the air–soil interface. Each trace of the radargram is transformed in the frequency domain over the band [200, 600] MHz with a step of 50 MHz and later corrupted by additive white Gaussian noise (AWGN) with a signal-to-noise-ratio equal to 0 dB.

The constant depth slices of the 3-D normalized tomographic reconstruction are displayed in Fig. 13 for the single target scenario when $h = 1$ m and $\varepsilon_{\mathrm{rs}} = 4$. As shown, the inversion of the proposed ray-based scattering model allows a correct target localization since the reconstruction peaks at $z = 0.5$ m at the upper target surface. Note that, due to

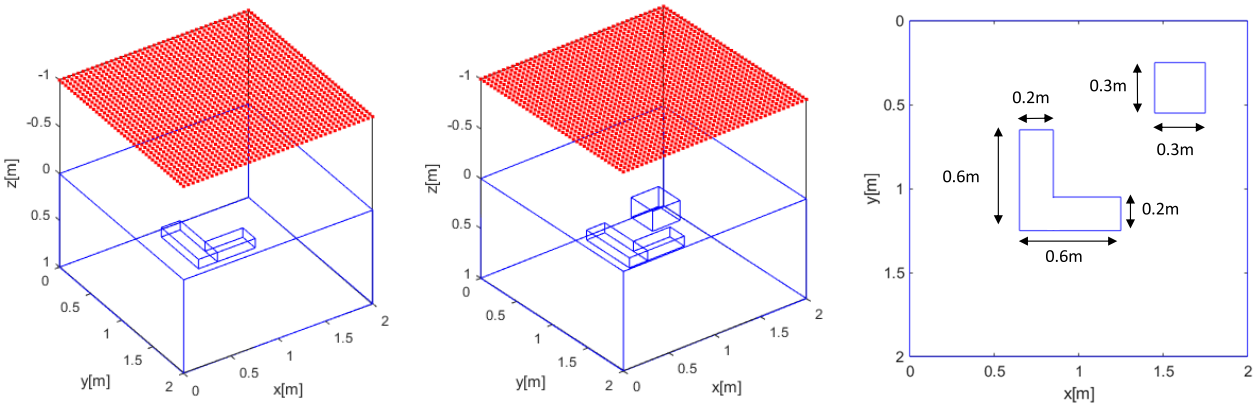

Fig. 12. (Left) Single target scenario. (Middle) Two-targets scenario. (Right) Dimensions of the targets in the *xy* plane.

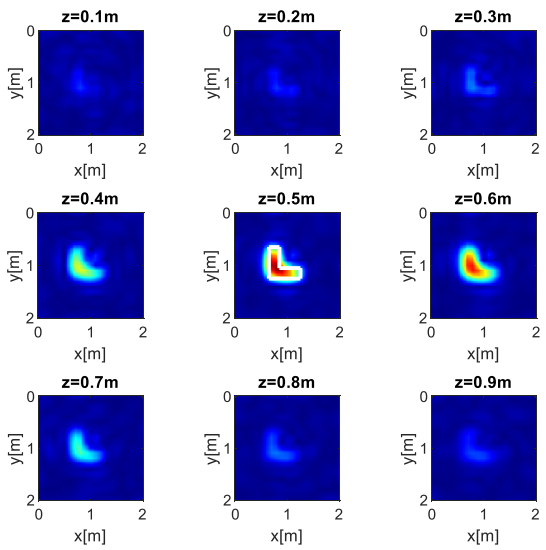

Fig. 13. Depth slices of the full-3-D tomographic reconstruction referred to the single target scenario for $h = 1$ m and $\varepsilon_{rs} = 4$. Color scale [0, 1].

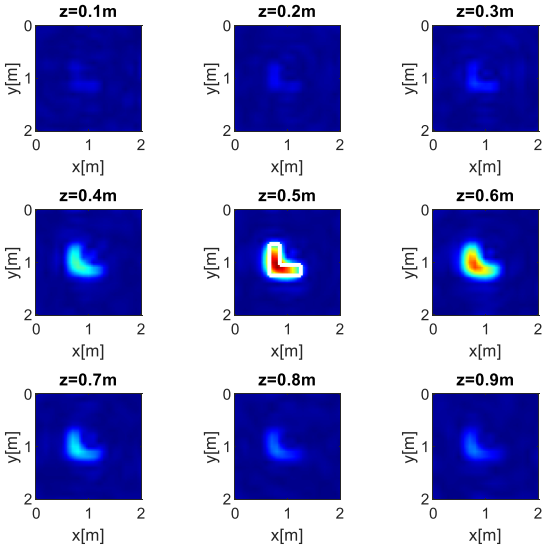

Fig. 14. Depth slices of the full-3-D tomographic reconstruction referred to the single target scenario for $h = 1$ m and $\varepsilon_{rs} = 6$. Color scale [0, 1].

the depth resolution limit (see Table I), the response from the lower target interface combines with the upper surface one. However, given the resolution limits, the target shape is identified in a quite satisfactory way.

The tomographic images depicted in Fig. 14 refer to the single target scenario when $h = 1$ m and $\varepsilon_{rs} = 6$. In agreement with the resolution data listed in Table I, it is noticed that the increased permittivity value has no tangible effects on the reconstruction quality in the horizontal plane. Conversely, the resolution slightly enhances along z since the energy of the reconstruction is reduced compared to Fig. 13 in the depth slices where no target is present.

Figs. 15 and 16 display the tomographic images of the single target scenario when $h = 2$ m for both permittivity values. When comparing these images with Figs. 13 and 14, the target is still correctly localized but the increase of the measurement quota has a detrimental effect on the horizontal resolution and, consequently, the target shape is not well recognizable.

To compare the focusing of the reconstructions in Figs. 13–16 in a more quantitative way, we evaluate their entropy E according to the definition reported in [35] here extended to the 3-D case, i.e.,

$$E = -\sum_{q=1}^{Q} \mathrm{ss}(x_q, y_q, z_q) \ln\left(\mathrm{ss}(x_q, y_q, z_q)\right) \tag{36}$$

where

$$\mathrm{ss}(x_q, y_q, z_q) = \frac{\left|\tilde{\chi}(x_q, y_q, z_q)\right|^2}{\sum_{q=1}^{Q}\left|\tilde{\chi}(x_q, y_q, z_q)\right|^2} \tag{37}$$

is the normalized square amplitude of the reconstructed contrast function at voxel (x_q, y_q, z_q), and Q is the total number of voxels in the tomographic image. The entropy in (36) is an indicator of the focusing of an image, and it has a higher value when the image has a poorer resolution.

Table III summarizes the entropy values of the reconstructions of the single target scenario (Figs. 13–16). These values confirm the superior focusing performance (lower entropy) achieved when the measurement grid is closer to the air–soil interface for a given soil permittivity. Furthermore, at a fixed measurement quota, increasing the soil permittivity slightly improves the image focusing.

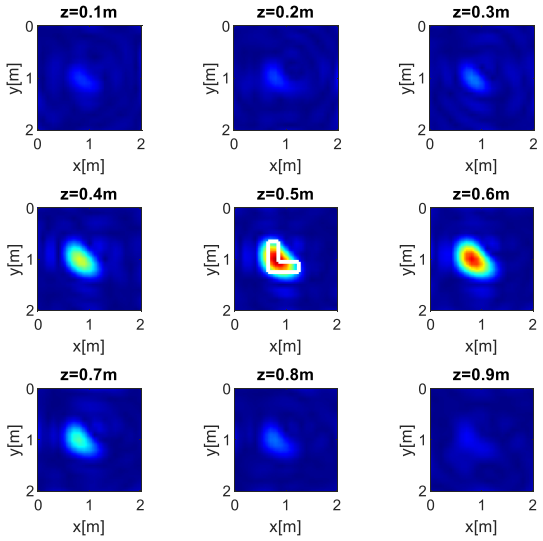

Fig. 15. Depth slices of the full-3-D tomographic reconstruction referred to the single target scenario for $h = 2$ m and $\varepsilon_{\mathrm{rs}} = 4$. Color scale [0, 1].

TABLE III
ENTROPY VALUES FOR THE TOMOGRAPHIC RECONSTRUCTIONS OF THE SINGLE TARGET SCENARIO

Case	Entropy
h=1 m, ε_{rs}=4	6.19
h=1 m, ε_{rs}=6	6.09
h=2 m, ε_{rs}=4	6.39
h=2 m, ε_{rs}=6	6.23

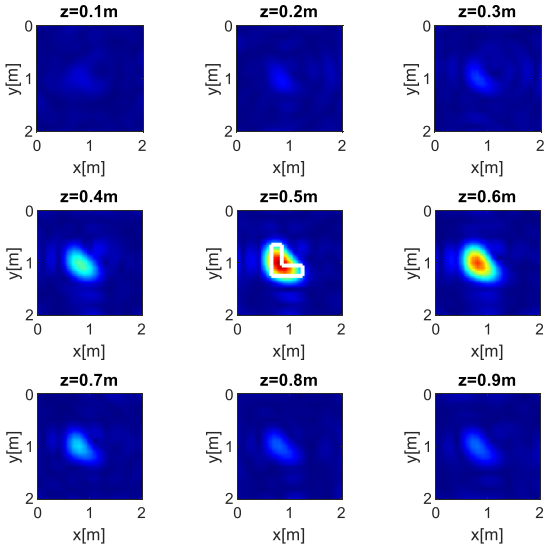

Fig. 16. Depth slices of the full-3-D tomographic reconstruction referred to the single target scenario for $h = 2$ m and $\varepsilon_{\mathrm{rs}} = 6$. Color scale [0, 1].

Tomographic reconstructions have been produced also for the more challenging two-targets scenario shown in the middle panel of Fig. 12. In this case, the measurement quota is fixed at $h = 1$ m and $\varepsilon_{\mathrm{rs}} = 4$. Furthermore, a soil electric conductivity ($\sigma = 0.01$ S/m) is introduced in the numerical simulator to account for GPR signal attenuation. In this regard, it must be stressed that despite the scattering model of (23) has been formally derived under the assumption of a lossless

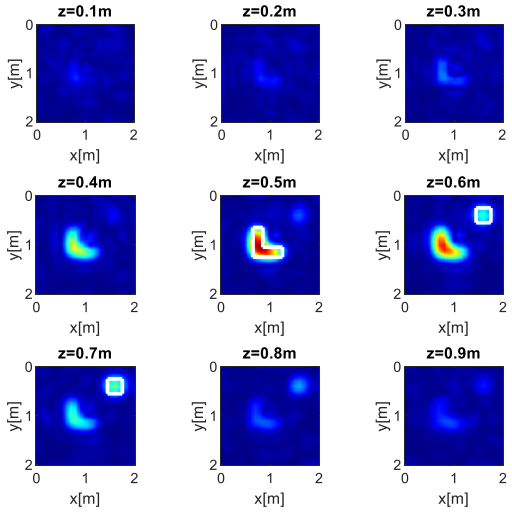

Fig. 17. Depth slices of the full-3-D tomographic reconstruction referred to the two-targets scenario. Line spacing 5 cm. Color scale [0, 1].

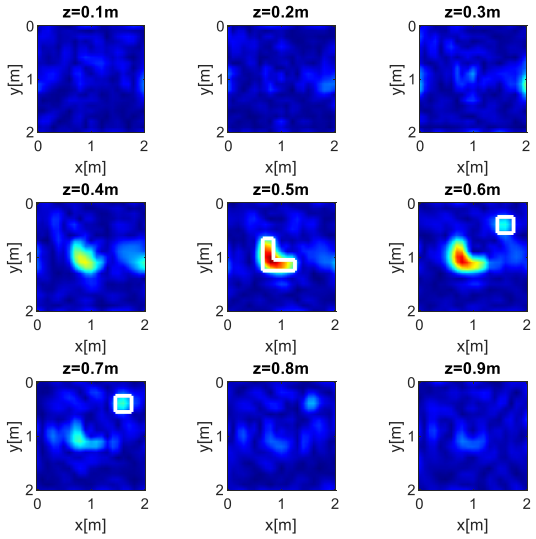

Fig. 18. Depth slices of the full-3-D tomographic reconstruction referred to the two-targets scenario. Line spacing 40 cm. Color scale [0, 1].

soil to simplify the analytical derivation, in the following we show that it can be successfully applied to process also data collected in the presence of a lossy soil. This claim is due to the fact only a qualitative reconstruction (i.e., the target support) is provided by a linearized inversion strategy and is supported by several numerical and experimental tests carried out by Catapano et al. [27], e.g., in relation to UAV GPR imaging [18], archeological prospections [27], and GPR imaging of tree trunks [36], [37].

Fig. 17 displays the full 3-D-tomographic reconstruction achieved by considering a spacing between the lines equal to 5 cm. It is observed that both targets are identified by the reconstruction procedure, with the L-shaped object providing a stronger response due to its larger radar cross section. To investigate the effect of the line spacing on the reconstruction capabilities, we have repeated the processing by increasing the spacing between the lines to 40 cm (i.e., six lines). The achieved results illustrated in Fig. 18 highlight that

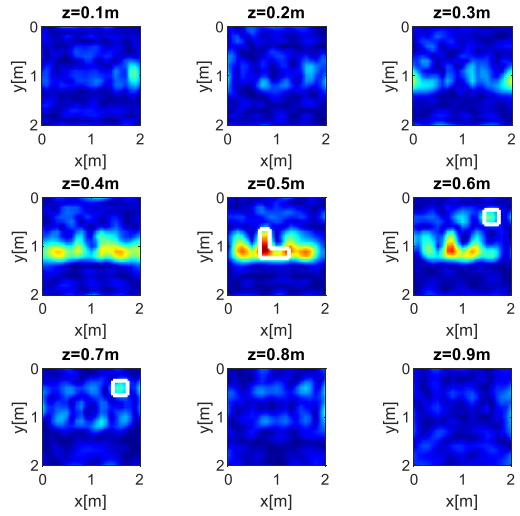

Fig. 19. Depth slices of the full-3-D tomographic reconstruction referred to the two-targets scenario. Line spacing 80 cm. Color scale [0, 1].

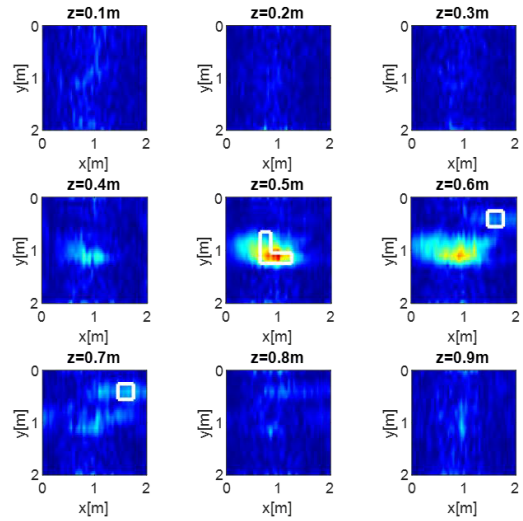

Fig. 20. Depth slices of the pseudo-3-D tomographic reconstruction referred to the two-targets scenario. Line spacing 5 cm. Color scale [0, 1].

a wider spacing introduces some artifacts in the images. This phenomenon is remarkable for a spacing of 80 cm (three lines) as shown in Fig. 19, where the presence of grating lobes due to the coarse spacing (see [38]) impairs the correct identification of the targets.

As a final test, the reconstruction performance of the full 3-D approach proposed in this work is compared with a pseudo-3-D imaging approach (e.g., see [27]). Pseudo-3-D imaging refers to a reconstruction strategy combining several 2-D reconstructions, whose number is equal to the number of measurement lines. As confirmed in Fig. 20 obtained for a line spacing equal to 5 cm, the targets are reconstructed only in part with the pseudo-3-D imaging strategy. This result agrees with the findings in [27] and confirms the importance of a full-3-D approach to get reliable images of the scene under investigation.

The computation complexity of the proposed reconstruction approach is linked to the construction of the forward scattering operator $\mathcal{P}$, based on the IRP computation, and the evaluation of its SVD. The inversion algorithm has been implemented under MATLAB 2020b on a Desktop PC equipped with an INTEL XEON GOLD 6136 CPU (3.0 GHz clock frequency) and 256 GB RAM. The computation times and memory requirements related to the operator and SVD calculations are summarized in Table IV. From the data in the table, it is concluded that most processing time is related to the IRP computation, whereas the memory occupation is mainly due to the operator and SVD computation.

TABLE IV
COMPUTATIONAL LOAD OF THE RECONSTRUCTION APPROACH

	IRP + operator computation	TSVD	Total
Computation time [s]	11942.8+58.6	576.3	12577.7
Memory occupation [GByte]	0.25+2.24	4.3	6.79

V. CONCLUSION

The article has proposed a full-3-D contactless GPR imaging approach based on the solution of a linearized inverse scattering problem. The approach relies on a ray-based model, which accounts for the radar signal propagation into a half-space scenario allowing an accurate evaluation of the kernel of the scattering equation to be inverted. A detailed analysis of the achievable resolution performance has been carried out for a measurement grid made by several parallel lines. To this aim, DT concepts and the SVD tool have been exploited. The effectiveness of the imaging strategy has been verified by processing full-wave synthetic data in the presence of various extended subsurface targets.

Future research activities will regard the experimental validation of the proposed imaging approach; the comparison with other focusing techniques, an in-depth study of the reconstruction performance in the case of incomplete or missing data. Regarding this latter point, the analytical results for the 2-D case provided in [2] and those for the 3-D homogeneous case given in [39] will be extended to the problem at hand. A further future activity will account for the analysis of measurement geometries different from the planar grid.

APPENDIX A
IRP COMPUTATION

This appendix deals with the determination of the IRP. With reference to Fig. 2, we rewrite the second Snell's law as

$$\sqrt{1-\cos^2\delta^i} = \sqrt{\varepsilon_{\rm rs}}\sqrt{1-\cos^2\delta^t} \tag{A1}$$

which leads to the equation

$$R_t^2\left(R_i^2-h^2\right) = \varepsilon_{\rm rs}R_i^2\left(R_t^2-z^2\right). \tag{A2}$$

In (A2), all quantities are known save for the IRP coordinates $(\tilde{x}, \tilde{y})$, which appear in the definition of the distances R_i and R_t [see (2) and (3)]. Hence, a further equation is needed

to work out the reflection point. Such an equation is obtained by imposing that the IRP belongs to the incidence plane Π_i.

The equation of Π_i is expressed in the canonical form

$$\Pi_i : ax + by + cz + d = 0 \tag{A3}$$

where a, b, and c are the components of the vector normal to the plane. By definition, the unit vector $\hat{\mathbf{e}}_\perp$ in (8) is normal to Π_i and so (A3) rewrites as

$$\frac{y_m - \tilde{y}}{R_i} x - \frac{x_m - \tilde{x}}{R_i} y + d = 0. \tag{A4}$$

Since the IRP must belong to Π_i, we plug its coordinates into (A4) to derive the coefficient d

$$d = \frac{1}{R_i}\left[\left(x_m - \tilde{x}\right)\tilde{y} - \left(y_m - \tilde{y}\right)\tilde{x}\right] \tag{A5}$$

which substituted into (A4) gives

$$(\tilde{y} - y_m)x - (\tilde{x} - x_m)y - x_m\tilde{y} + y_m\tilde{x} = 0. \tag{A6}$$

Finally, (A2) and (A6) form a non-linear equation system

$$\begin{cases} R_t^2\left(R_i^2 - h^2\right) = \varepsilon_{\mathrm{rs}} R_i^2\left(R_t^2 - z^2\right) \\ (\tilde{y} - y_m)x - (\tilde{x} - x_m)y - x_m\tilde{y} + y_m\tilde{x} = 0 \end{cases} \tag{A7}$$

wherein the IRP coordinates $\left(\tilde{x}, \tilde{y}\right)$ are the two unknowns.

Appendix B
Determination of the Transmitted Field and Inhomogeneous Green's Function

A Hertzian dipole directed along $\mathbf{u}_{\mathrm{tx}}$ radiates an electric field [29]

$$\mathbf{E}^i\left(\tilde{\mathbf{r}}\right) = -j\omega\mu_0 \underline{\underline{\mathbf{G}}}^1\left(\tilde{\mathbf{r}}, \mathbf{r}_m\right) \cdot \mathbf{u}_{\mathrm{tx}} \tag{B1}$$

where $\underline{\underline{\mathbf{G}}}^1$ is the dyadic Green's function in free-space accounting for radiation from $\mathbf{r_m}$ to $\tilde{\mathbf{r}}$ [31]. Equations (B2)–(B4), as shown at the bottom of the page.

Under the far-field approximation ($k_0 h \gg 1$), the functions G_1 and G_2 are approximated as

$$G_1 \approx \frac{1}{4\pi R_i} \tag{B5}$$

$$G_2 = -\frac{1}{4\pi R_i^3} \tag{B6}$$

and then (B2) rewrites as equation (B7), shown at the bottom of the page.

Now, we substitute (B7) into (B1) to get the expression of the incident field at the IRP

$$\mathbf{E}^i\left(\tilde{\mathbf{r}}\right) = -j\omega\mu_0 \underline{\underline{\tilde{\mathbf{G}}}}^1 \cdot \mathbf{u}_{\mathrm{tx}} \frac{e^{-jk_0 R_i}}{4\pi R_i} \tag{B8}$$

that is plugged into (17) to find the transmitted field in the subsoil at the observation point $\mathbf{r}$, i.e.,

$$\mathbf{E}^t(\mathbf{r}, \mathbf{r}_m) - j\omega\mu_0 \underline{\underline{\mathbf{M}}}_1 \cdot \underline{\underline{\mathbf{T}}} \cdot \underline{\underline{\mathbf{M}}}_2 \cdot \underline{\underline{\tilde{\mathbf{G}}}}^1 \cdot \mathbf{u}_{\mathrm{tx}} \frac{e^{-jk_0\left(R_i + \sqrt{\varepsilon_{\mathrm{rs}}} R_t\right)}}{4\pi\left(R_i + R_t\right)}. \tag{B9}$$

Similar to (B1), we rewrite (B9) as

$$\mathbf{E}^t(\mathbf{r}, \mathbf{r}_m) = -j\omega\mu_0 \underline{\underline{\mathbf{G}}}^{12}(\mathbf{r}, \mathbf{r}_m) \cdot \boldsymbol{u}_{\mathrm{tx}} \tag{B10}$$

where

$$\underline{\underline{\mathbf{G}}}^{12}(\mathbf{r}, \mathbf{r}_m) = \underline{\underline{\mathbf{M}}}_1 \cdot \underline{\underline{\mathbf{T}}} \cdot \underline{\underline{\mathbf{M}}}_2 \cdot \underline{\underline{\tilde{\mathbf{G}}}}^1 \frac{e^{-jk_0\left(R_i + \sqrt{\varepsilon_{\mathrm{rs}}} R_t\right)}}{4\pi\left(R_i + R_t\right)} \tag{B11}$$

is the inhomogeneous Green's function of the scenario accounting for the radiation of a Hertzian dipole from region 1 to region 2.

Due to the symmetry property of dyadic Green's functions [29], the inhomogeneous dyadic Green's function $\underline{\underline{\mathbf{G}}}^{21}$ from region 2 to region 1 appearing in (4) is given by

$$\begin{aligned} \underline{\underline{\mathbf{G}}}^{21}(\mathbf{r}_m, \mathbf{r}) &= \left[\underline{\underline{\mathbf{G}}}^{12}(\mathbf{r}, \mathbf{r}_m)\right]^T \\ &= \underline{\underline{\tilde{\mathbf{G}}}}^{1\mathrm{T}} \cdot \underline{\underline{\mathbf{M}}}_2^T \cdot \underline{\underline{\mathbf{T}}}^T \cdot \underline{\underline{\mathbf{M}}}_1^T \frac{e^{-jk_0\left(R_i + \sqrt{\varepsilon_{\mathrm{rs}}} R_t\right)}}{4\pi\left(R_i + R_t\right)} \end{aligned} \tag{B12}$$

where T denotes the transpose operation.

$$\underline{\underline{\mathbf{G}}}^1\left(\tilde{\mathbf{r}}, \mathbf{r}_m\right) = e^{-jk_0 R_i} \cdot \begin{bmatrix} G_1 + G_2\left(\tilde{x} - x_m\right)^2 & G_2\left(\tilde{x} - x_m\right)\left(\tilde{y} - y_m\right) & G_2\left(\tilde{x} - x_m\right)h \\ G_2\left(\tilde{x} - x_m\right)\left(\tilde{y} - y_m\right) & G_1 + G_2\left(\tilde{y} - y_m\right)^2 & G_2\left(\tilde{y} - y_m\right)h \\ G_2\left(\tilde{x} - x_m\right)h & G_2\left(\tilde{y} - y_m\right)h & G_1 + G_2 h^2 \end{bmatrix} \tag{B2}$$

$$G_1 = \frac{-1 - jk_0 R_i + k_0^2 R_i^2}{4\pi k_0^2 R_i^3} \tag{B3}$$

$$G_2 = \frac{3 + j3k_0 R_i - k_0^2 R_i^2}{4\pi k_0^2 R_i^5} \tag{B4}$$

$$\begin{aligned} \underline{\underline{\mathbf{G}}}^1\left(\tilde{\mathbf{r}}, \mathbf{r}_m\right) &= \begin{bmatrix} 1 - \frac{\left(\tilde{x} - x_m\right)^2}{R_i^2} & -\frac{\left(\tilde{x} - x_m\right)\left(\tilde{y} - y_m\right)}{R_i^2} & -\frac{\left(\tilde{x} - x_m\right)h}{R_i^2} \\ -\frac{\left(\tilde{x} - x_m\right)\left(\tilde{y} - y_m\right)}{R_i^2} & 1 - \frac{\left(\tilde{y} - y_m\right)^2}{R_i^2} & -\frac{\left(\tilde{y} - y_m\right)h}{R_i^2} \\ -\frac{\left(\tilde{x} - x_m\right)h}{R_i^2} & -\frac{\left(\tilde{y} - y_m\right)h}{R_i^2} & 1 - \frac{h^2}{R_i^2} \end{bmatrix} \frac{e^{-jk_0 R_i}}{4\pi R_i} \\ &= \underline{\underline{\tilde{\mathbf{G}}}}^1 \frac{e^{-jk_0 R_i}}{4\pi R_i} \end{aligned} \tag{B7}$$

REFERENCES

[1] D. J. Daniels, *Ground Penetrating Radar*. Hoboken, NJ, USA: Wiley, 2005.

[2] R. Persico, *Introduction to Ground Penetrating Radar: Inverse Scattering and Data Processing*. Hoboken, NJ, USA: Wiley, 2014.

[3] I. Catapano, G. Gennarelli, G. Ludeno, F. Soldovieri, and R. Persico, "Ground-penetrating radar: Operation principle and data processing," in *Wiley Encyclopedia of Electrical and Electronics Engineering*. 2019, pp. 1–23.

[4] N. Diamanti and A. P. Annan, "Air-launched and ground-coupled GPR data," in *Proc. 11th Eur. Conf. Antennas Propag. (EUCAP)*, Paris, France, Mar. 2017, pp. 1694–1698.

[5] A. Benedetto, F. Tosti, L. B. Ciampoli, and F. D'Amico, "An overview of ground-penetrating radar signal processing techniques for road inspections," *Signal Process.*, vol. 132, pp. 201–209, Mar. 2017.

[6] I. Trinks et al., "Large-area high-resolution ground-penetrating radar measurements for archaeological prospection," *Archaeol. Prospection*, vol. 25, no. 3, pp. 171–195, 2018.

[7] D. W. Paglieroni, D. H. Chambers, J. E. Mast, S. W. Bond, and N. R. Beer, "Imaging modes for ground penetrating radar and their relation to detection performance," *IEEE J. Sel. Topics Appl. Earth Observ. Remote Sens.*, vol. 8, no. 3, pp. 1132–1144, Mar. 2015.

[8] F. Soldovieri, G. Gennarelli, I. Catapano, D. Liao, and T. Dogaru, "Forward-looking radar imaging: A comparison of two data processing strategies," *IEEE J. Sel. Topics Appl. Earth Observ. Remote Sens.*, vol. 10, no. 2, pp. 562–571, Feb. 2017.

[9] D. Comite, F. Ahmad, M. G. Amin, and T. Dogaru, "Forward-looking ground-penetrating radar: Subsurface target imaging and detection: A review," *IEEE Geosci. Remote Sens. Mag.*, vol. 9, no. 4, pp. 173–190, Dec. 2021.

[10] F. Rodriguez-Morales et al., "Advanced multifrequency radar instrumentation for polar research," *IEEE Trans. Geosci. Remote Sens.*, vol. 52, no. 5, pp. 2824–2842, May 2014.

[11] I. Catapano, L. Crocco, Y. Krellmann, G. Triltzsch, and F. Soldovieri, "A tomographic approach for helicopter-borne ground penetrating radar imaging," *IEEE Geosci. Remote Sens. Lett.*, vol. 9, no. 3, pp. 378–382, May 2012.

[12] G. Gennarelli et al., "A low frequency airborne GPR system for wide area geophysical surveys: The case study of Morocco desert," *Remote Sens. Environ.*, vol. 233, Nov. 2019, Art. no. 111409.

[13] R. Croci, R. Seu, E. Flamini, and E. Russo, "The shallow radar (SHARAD) onboard the NASA MRO mission," *Proc. IEEE*, vol. 99, no. 5, pp. 794–807, May 2011.

[14] R. Orosei et al., "Radar evidence of subglacial liquid water on Mars," *Science*, vol. 361, no. 6401, pp. 490–493, 2018.

[15] G. Ludeno, I. Catapano, A. Renga, A. R. Vetrella, G. Fasano, and F. Soldovieri, "Assessment of a micro-UAV system for microwave tomography radar imaging," *Remote Sens. Environ.*, vol. 212, pp. 90–102, Jun. 2018.

[16] M. G. Fernández et al., "Synthetic aperture radar imaging system for landmine detection using a ground penetrating radar on board a unmanned aerial vehicle," *IEEE Access*, vol. 6, pp. 45100–45112, 2018.

[17] Y. A. López, M. García-Fernández, G. Álvarez-Narciandi, and F. L.-H. Andrés, "Unmanned aerial vehicle-based ground-penetrating radar systems: A review," *IEEE Geosci. Remote Sens. Mag.*, vol. 10, no. 2, pp. 66–86, Jun. 2022.

[18] C. Noviello et al., "An overview on down-looking UAV-based GPR systems," *Remote Sens.*, vol. 14, no. 14, p. 3245, Jul. 2022.

[19] M. Ambrosanio, M. T. Bevacqua, T. Isernia, and V. Pascazio, "Performance analysis of tomographic methods against experimental contactless multistatic ground penetrating radar," *IEEE J. Sel. Topics Appl. Earth Observ. Remote Sens.*, vol. 14, pp. 1171–1183, 2021.

[20] I. Catapano, G. Gennarelli, G. Ludeno, C. Noviello, G. Esposito, and F. Soldovieri, "Contactless ground penetrating radar imaging: State of the art, challenges, and microwave tomography-based data processing," *IEEE Geosci. Remote Sens. Mag.*, vol. 10, no. 1, pp. 251–273, Mar. 2022.

[21] R. H. Stolt, "Migration by Fourier transform," *Geophysics*, vol. 43, no. 1, pp. 23–48, Feb. 1978.

[22] X. Feng and M. Sato, "Pre-stack migration applied to GPR for landmine detection," *Inverse Problems*, vol. 20, no. 6, pp. S99–S115, Dec. 2004.

[23] A. J. Devaney, "Geophysical diffraction tomography," *IEEE Trans. Geosci. Remote Sens.*, vol. GE-22, no. 1, pp. 3–13, Jan. 1984.

[24] T. J. Cui and W. C. Chew, "Diffraction tomographic algorithm for the detection of three-dimensional objects buried in a lossy half-space," *IEEE Trans. Antennas Propag.*, vol. 50, no. 1, pp. 42–49, Jan. 2002.

[25] R. Solimene, I. Catapano, G. Gennarelli, A. Cuccaro, A. Dell'Aversano, and F. Soldovieri, "SAR imaging algorithms and some unconventional applications: A unified mathematical overview," *IEEE Signal Process. Mag.*, vol. 31, no. 4, pp. 90–98, Jul. 2014.

[26] G. Gennarelli, I. Catapano, F. Soldovieri, and R. Persico, "On the achievable imaging performance in full 3-D linear inverse scattering," *IEEE Trans. Antennas Propag.*, vol. 63, no. 3, pp. 1150–1155, Mar. 2015.

[27] I. Catapano, A. Affinito, G. Gennarelli, F. di Maio, A. Loperte, and F. Soldovieri, "Full three-dimensional imaging via ground penetrating radar: Assessment in controlled conditions and on field for archaeological prospecting," *Appl. Phys. A, Solids Surf.*, vol. 115, no. 4, pp. 1415–1422, Jun. 2014.

[28] M. Bertero and P. Boccacci, *Introduction to Inverse Problems in Imaging*. Bristol, U.K.: Institute of Physics Publishing, 1998.

[29] W. C. Chew, *Waves and Fields in Inhomogeneous Media*. Piscataway, NJ, USA: Institute of Electrical and Electronics Engineers, 1995.

[30] G. Ludeno, G. Gennarelli, S. Lambot, F. Soldovieri, and I. Catapano, "A comparison of linear inverse scattering models for contactless GPR imaging," *IEEE Trans. Geosci. Remote Sens.*, vol. 58, no. 10, pp. 7305–7316, Oct. 2020.

[31] C. A. Balanis, *Advanced Engineering Electromagnetics*. New York, NY, USA: Wiley, 2012.

[32] T. Negishi, G. Gennarelli, F. Soldovieri, Y. Liu, and D. Erricolo, "Radio frequency tomography for nondestructive testing of pillars," *IEEE Trans. Geosci. Remote Sens.*, vol. 58, no. 6, pp. 3916–3926, Jun. 2020.

[33] M. J. D. Powell, "A Fortran subroutine for solving systems of nonlinear algebraic equations," At. Energy Res. Establishment, Harwell, U.K., 1968.

[34] C. Warren, A. Giannopoulos, and I. Giannakis, "gprMax: Open source software to simulate electromagnetic wave propagation for ground penetrating radar," *Comput. Phys. Commun.*, vol. 209, pp. 163–170, Dec. 2016.

[35] G. Gennarelli and F. Soldovieri, "Performance analysis of incoherent RF tomography using wireless sensor networks," *IEEE Trans. Geosci. Remote Sens.*, vol. 54, no. 5, pp. 2722–2732, May 2016.

[36] A. M. Alani et al., "The use of ground penetrating radar and microwave tomography for the detection of decay and cavities in tree trunks," *Remote Sens.*, vol. 11, no. 18, p. 2073, Sep. 2019.

[37] F. Tosti et al., "The use of GPR and microwave tomography for the assessment of the internal structure of hollow trees," *IEEE Trans. Geosci. Remote Sens.*, vol. 60, 2022, Art. no. 2002314.

[38] G. Gennarelli, I. Catapano, and F. Soldovieri, "Reconstruction capabilities of down-looking airborne GPRs: The single frequency case," *IEEE Trans. Comput. Imag.*, vol. 3, no. 4, pp. 917–927, Dec. 2017.

[39] C. Noviello, G. Esposito, I. Catapano, and F. Soldovieri, "Multilines imaging approach for mini-UAV radar imaging system," *IEEE Geosci. Remote Sens. Lett.*, vol. 19, pp. 1–5, 2022.

Gianluca Gennarelli received the M.Sc. degree (summa cum laude) in electronic engineering and the Ph.D. degree in information engineering from the University of Salerno, Salerno, Italy, in 2006 and 2010, respectively.

From 2010 to 2011, he was a Post-Doctoral Fellow at the University of Salerno. Since 2012, he has been a Research Scientist with the Institute for Electromagnetic Sensing of the Environment, National Research Council of Italy (IREA-CNR), Naples, Italy. In 2015, he was a Visiting Scientist with the NATO-CMRE, La Spezia, Italy. He has coauthored over a 100 publications in international peer-reviewed journals and conference proceedings and he serves as a reviewer for several international journals and conference papers. His research interests include microwave sensors, antennas, inverse scattering problems, radar imaging and signal processing, diffraction problems, and electromagnetic simulation.

Carlo Noviello (Member, IEEE) received the M.S. and Ph.D. degrees in telecommunication engineering from the University of Naples Federico II, Naples, Italy, in 2011 and 2015, respectively.

Since 2012, he has been collaborating with the Institute for Electromagnetic Sensing of the Environment (IREA), National Research Council of Italy (IREA-CNR), Naples, where he is currently an Associate Researcher. His research interests include statistical radar signal processing, with emphasis on of unmanned aerial vehicle (UAV), airborne and spaceborne platforms, synthetic aperture radar (SAR) interferometry, and inverse SAR imaging techniques.

Dr. Noviello takes part in the most important Scientific Conference in the Remote Sensing field of context and also serves as a regular referee for the main IEEE scientific journals.

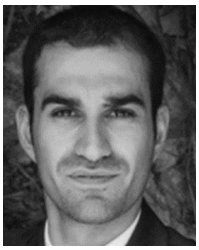

Giovanni Ludeno received the M.S. degree in telecommunication engineering from the University "Mediterranea" of Reggio Calabria, Reggio Calabria, Italy, in 2011, and the Ph.D. degree in electronics and computer engineering from the University of Campania "Luigi Vanvitelli," Caserta, Italy, in 2015.

From November 2011 to October 2012, he was a Scholar with the Institute for Electromagnetic Sensing of the Environment, National Research Council of Italy (IREA-CNR), Naples, Italy. From October 2012 to January 2014, he was a Research Fellow with Vitrociset SpA, Rome, Italy. Since 2015, he has been a Research Scientist with IREA-CNR, Naples. He has coauthored over 60 publications in international peer-reviewed journals, conference proceedings, and books. His research interests include the field of applied electromagnetism, with special regard to remote and in situ sensing.

Dr. Ludeno was the Guest Editor for special issue in *Journal of Marine Science of Engineering* (MDPI) of which now is a Topic Editor.

Giuseppe Esposito received the M.Sc. degree (summa cum laude) in aerospace engineering and the Ph.D. degree in industrial engineering from the University of Naples Federico II, Naples, Italy, in 2018 and 2023, respectively.

Since 2019, he has been collaborating with the Institute for Electromagnetic Sensing of the Environment (IREA), of the National Research Council of Italy (CNR), Naples. From May to July 2022, he was a Visiting Researcher at the University of Illinois at Chicago (UIC), Chicago, IL, USA. His research interests include the field of unmanned aerial vehicle-based radar imaging, with emphasis on platform positioning, data synchronization, sensor fusion, and inverse scattering approaches.

Francesco Soldovieri has been the Scientific Coordinator of the FP7 projects ISTIMES and AMISS and the Technical Manager of the H2020 Project HERACLES. He has been the President of the Division on Geosciences Instrumentation and Data Systems of European Geosciences Union. He is a Research Director at the Institute for Electromagnetic Sensing of the Environment, National Research Council of Italy (CNR), Naples, Italy. He is the coauthor of about 240 articles on national and international journals and more than 350 conference proceedings. His research interests include radar imaging, data processing for ground penetrating radar (GPR), indoor surveillance, through-wall imaging, passive radars, integration of geophysical data, radars for planetary exploration.

Dr. Soldovieri was a member of the Editorial Board of IEEE-GRSL and now of IEEE-TCI and IEEE-TGRS, *Remote Sensing* (MDPI). He was the General Chair of the International Workshop on Advanced Ground Penetrating Radar 2007 and the General Co-Chair of the Ground Penetrating Radar Conference 2010. He is the Editor-in-Chief of HERITAGE, an MDPI journal devoted to Cultural and Natural Heritage.

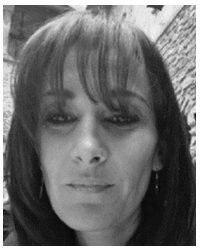

Ilaria Catapano (Member, IEEE) received the Ph.D. degree in electrical and information engineering from the University of Cassino, Cassino, Italy, in 2006.

In 2003, she started her research activity at the Institute for Electromagnetic Sensing of the Environment, National Research Council of Italy (IREA-CNR), Naples, Italy. She is a Research Scientist at CNR, level II. Her skills are about electromagnetic modeling, forward and inverse scattering problems, remote and in situmicrowave, and teraHertz (THz) sensing techniques. She has published more than 170 published articles with about 90 international journal articles. Her research interests include radar imaging with a focus on processing of experimental data gathered by means of ground-based, airborne and drone radar systems, THz spectroscopy and imaging, measurement campaigns carried out by means of microwave and THz devices, development of high-frequency radar systems and data processing strategies for target detection and tracking and vital signs monitoring, and use of microwaves and THz for food inspections and medical imaging.

Dr. Catapano received the Giorgio Barzilai Award by the Italian Electromagnetic Society (SIEM), in 2004, was one of the Young Scientist Awardees at the XXIX URSI General Assembly, in 2008, an Adjunct Professor at Mediterranea University, Reggio Calabria, Italy, in 2010, and an Invited Lecturer at Sao Paulo University, São Paulo, Brazil, in 2013, and the Indian Institute of Technology, Kharagpur, India, in 2016. She is an Associate Editor of IEEE TRANSACTIONS ON COMPUTATIONAL IMAGING and a referee for many international journals.

Open Access funding provided by 'Consiglio Nazionale delle Ricerche-CARI-CARE' within the CRUI CARE Agreement